

Floquet-Engineering Weyl Points and Linked Fermi Arcs from Straight Nodal Lines

Dongling Liu,¹ Zheng-Yang Zhuang,¹ and Zhongbo Yan^{1,*}

¹Guangdong Provincial Key Laboratory of Magnetoelectric Physics and Devices,
State Key Laboratory of Optoelectronic Materials and Technologies,
School of Physics, Sun Yat-sen University, Guangzhou 510275, China
(Dated: July 8, 2025)

Floquet engineering provides a powerful and flexible method for modifying the band structures of quantum materials. While circularly polarized light has been shown to convert curved nodal lines in three-dimensional semimetals into Weyl points, such a transformation is forbidden for an isolated straight nodal line. In this work, we uncover a dramatic shift in this paradigm when multiple straight nodal lines intersect. We observe that circularly polarized light not only gaps them into Weyl points but also induces unprecedented surface-state Fermi arcs that extend across the entire surface Brillouin zone and form a linked topological structure. These findings advance our fundamental understanding of light-driven transitions in topological semimetals and unveil a unique Weyl semimetal phase defined by linked Fermi arcs. We discuss potential exotic phenomena arising from this phase, applications of our predictions to spin-splitting antiferromagnets, and the extension of this Weyl semimetal phase to classical systems.

Introduction.—A groundbreaking advance in Floquet engineering emerged with the discovery that circularly polarized light (CPL) can open a band gap at graphene’s Dirac points [1], realizing topological gapped phases now known as Floquet Chern insulators. This seminal work ignited widespread investigation into Floquet topological phases [2–11] and light-driven topological phase transitions in quantum materials [12–15]. The direct observation of light-driven band structure modifications, however, was challenging for years until recent notable advances in time- and angle-resolved photoemission spectroscopy (TrARPES). This technique’s unprecedented capability to resolve photon-dressed band structure in momentum space [16–19] is now propelling the field into an exciting new phase of discovery.

Band degeneracy serves as the source for the nontrivial topological properties of the band structure [20]. The influence of CPL on band degeneracy depends critically on both the system’s dimension and the structure of the degeneracy. In two-dimensional (2D) systems, the most common type of band degeneracy is Dirac points protected by \mathcal{PT} symmetry. Since CPL generally breaks \mathcal{PT} symmetry, 2D Dirac points are unstable under CPL irradiation. Consequently, the 2D Floquet topological phases induced by CPL typically exhibit gapped band structures [21–23]. In three-dimensional (3D) systems, band degeneracies exhibit greater diversity, encompassing nodal points [24–28], nodal lines [29–37], and nodal surfaces [38, 39]. This diversity leads to a richer interplay between CPL and band degeneracy compared to 2D systems. Among these band degeneracies, Weyl points are special because their stability is topologically protected [40], unlike other band degeneracies that rely on symmetry protection. When subjected to CPL, Weyl points primarily experience chirality-dependent positional shifts [41], while other degeneracies typically transform into Weyl points [42–61]. This conversion results in a robust topological gapless phase—the Floquet Weyl semimetal. Particularly interesting is the transition from curved nodal lines to Weyl points [illustrated in Fig. 1(b)], which typically generates widely separated Weyl

points [44–46] and enables the realization of multi-Weyl points [48, 49]. This large separation leads to extended Fermi-arc surface states at the boundary and gives rise to pronounced anomalous Hall effects.

Crystalline symmetries can enforce nodal lines to be straight [62–70]. However, research on Floquet Weyl points (FWPs) arising from nodal lines has thus far been confined to curved cases [44–52]. This restriction stems from the fact that a straight nodal line (SNL) effectively represents a stack of 2D Dirac points along a specific momentum direction. Since these Dirac points are identical, CPL affects them uniformly—either gapping all of them simultaneously or leaving the entire stack unaffected (as demonstrated below). Consequently, this uniform response prevents the generation of FWPs from SNLs [illustrated in Fig. 1(c)]. In this work, we demonstrate that this paradigm undergoes a dramatic transformation when multiple SNLs intersect. Beyond the unexpected emergence of FWPs, we discover an extraordinary characteristic of the resulting Fermi-arc surface states: they span the entire surface Brillouin zone (BZ), forming an intricately linked structure—a phenomenon never before observed in either static or Floquet Weyl semimetals. This unprecedented feature originates from a nontrivial pattern in the layer Chern numbers. We note that linked Fermi loops have recently been experimentally realized in photonic 3D Chern insulators [71]. However, a crucial distinction exists between these fully gapped Chern insulators and our Floquet Weyl semimetals. In the former, the layer Chern numbers remain constant along a specific momentum direction, whereas in the latter, they exhibit sign reversal. We also investigate the anomalous Hall effect in this system, uncovering a strong dependence on the propagation direction of the incident light.

A single SNL under CPL irradiation.—To appreciate the striking difference between isolated and intersected SNLs, we first show the effect of CPL on an isolated SNL. Specially, we consider the following continuum model:

$$\mathcal{H}(\mathbf{k}) = k_y \sigma_x + k_z \sigma_y, \quad (1)$$

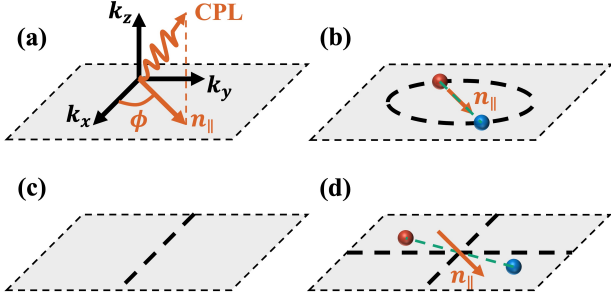


FIG. 1. Schematic diagram illustrating the influence of CPL on different types of nodal lines. Dashed black lines denote gapped nodal lines, while solid dots represent CPL-induced FWPs of opposite chirality (red/blue). (a) CPL is incident along a general direction. (b) Two FWPs emerge from a circular nodal ring, displaced along \mathbf{n}_{\parallel} (light's in-plane projection). (c) No FWPs emerge for an isolated SNL. (d) Two FWPs appear near two SNLs' crossing point, with their displacement vector generally non-parallel to \mathbf{n}_{\parallel} .

where $\mathbf{k} = (k_x, k_y, k_z)$. The energy spectra are given by $E_{\pm}(\mathbf{k}) = \pm \sqrt{k_y^2 + k_z^2}$, featuring a SNL along the k_x axis. We consider that CPL is incident in the direction $\mathbf{n} = (\cos \phi \sin \theta, \sin \phi \sin \theta, \cos \theta)$, where ϕ and θ are the azimuthal and polar angles in the spherical coordinate system [illustrated in Fig. 1(a)], respectively. The vector potential of the light is described by $\mathbf{A}(t) = A_0[\cos(\omega t)\mathbf{e}_1 + \eta \sin(\omega t)\mathbf{e}_2]$. Here, ω is the angular frequency and $\eta = \pm 1$ labels the two types of handedness. The two unit vectors, $\mathbf{e}_1 = (\sin \phi, -\cos \phi, 0)$ and $\mathbf{e}_2 = (\cos \phi \cos \theta, \sin \phi \cos \theta, -\sin \theta)$, are orthogonal and lie perpendicular to \mathbf{n} due to the light's transverse-wave nature.

The effect of CPL is incorporated through the minimal coupling, $\mathcal{H}(\mathbf{k}) \rightarrow \mathcal{H}(\mathbf{k} + e\mathbf{A})$, where e denotes the elementary charge and we take $e > 0$. We focus on the high-frequency off-resonant regime. According to the Floquet-Magnus theory, the system is effectively described by a time-independent Hamiltonian that is given by [72, 73]

$$\mathcal{H}_{\text{eff}}(\mathbf{k}) = \mathcal{H}_0(\mathbf{k}) + \sum_{n \geq 1} \frac{[\mathcal{H}_{+n}, \mathcal{H}_{-n}]}{n\omega} + O(\omega^{-2}), \quad (2)$$

where \mathcal{H}_n denotes the n th-decomposition coefficient matrix, i.e., $\mathcal{H}(\mathbf{k}, t) = \sum_n \mathcal{H}_n(\mathbf{k}) e^{in\omega t}$ with $n \in \mathbb{Z}$. For this Hamiltonian, we have $\mathcal{H}_0(\mathbf{k}) = k_y\sigma_x + k_z\sigma_y$ and $\mathcal{H}_{\pm 1}(\mathbf{k}) = -\frac{eA_0}{2}[(\cos \phi \pm i\eta \sin \phi \cos \theta)\sigma_x \mp i\eta \sin \theta \sigma_y]$, which yields:

$$\mathcal{H}_{\text{eff}}(\mathbf{k}) = k_y\sigma_x + k_z\sigma_y - \eta \frac{(eA_0)^2}{2\omega} \cos \phi \sin \theta \sigma_z. \quad (3)$$

It is readily seen that the SNL remains gapless only when the light is incident perpendicular to the SNL, corresponding to either $\theta = \{0, \pi\}$ or $\phi = \{\frac{\pi}{2}, \frac{3\pi}{2}\}$. In all other orientations, the SNL develops a gap. Notably, in contrast to curved nodal lines [44–46], FWPs never emerge in this system under any illumination conditions.

Although FWPs cannot be generated, fully gapping out the SNL instead results in a 3D Floquet Chern insulator character-

ized by layer Chern numbers $(C(k_x), C(k_y), C(k_z))$. Here, $C(k_i)$ denotes the layer Chern number defined on the 2D momentum plane with fixed k_i , given explicitly by $C(k_i) = \frac{1}{2\pi} \sum_{j,l} \epsilon_{ijl} \int dk_j dk_l \partial_j A_l$ where ϵ_{ijl} is the third-order anti-symmetry tensor, and $A_l = i\langle u(\mathbf{k}) | \partial_l u(\mathbf{k}) \rangle$ is the Berry connection of the occupied band. For the continuum Hamiltonian considered here, we find

$$(C(k_x), C(k_y), C(k_z)) = \left(\frac{\eta \text{sgn}(\cos \phi)}{2}, 0, 0 \right). \quad (4)$$

The half-integer value arises from the non-compact nature of the momentum space (every momentum plane belongs to \mathbb{R}^2). However, for lattice Hamiltonians where the BZ is a closed torus, the Chern number must be quantized to integers. This implies that SNLs with linear dispersion must appear in pairs in lattice systems—a direct consequence of the fermion doubling theorem [74].

Two intersected SNLs under CPL irradiation.—We now show how intersected SNLs lead to qualitatively new behavior. As the simplest example, we analyze two intersected SNLs, described by the Hamiltonian

$$\mathcal{H}(\mathbf{k}) = k_z\sigma_x + k_x k_y \sigma_y. \quad (5)$$

The two SNLs are located along the k_x and k_y axes and intersect at $\mathbf{k} = (0, 0, 0)$. Applying the Floquet-Magnus theory yields

$$\begin{aligned} \mathcal{H}_{\text{eff}}(\mathbf{k}) = & k_z\sigma_x + (k_x k_y - \frac{(eA_0)^2}{4} \sin 2\phi \sin^2 \theta) \sigma_y \\ & + \eta \frac{(eA_0)^2}{2\omega} \sin \theta (-\cos \phi k_x + \sin \phi k_y) \sigma_z. \end{aligned} \quad (6)$$

Depending on the direction of light, the fate of the two SNLs can be categorized into three cases: (i) $\theta = 0$ or π . The SNLs remain intact, as all driving-induced terms vanish. This aligns with the conclusion that an SNL is stable against CPL incident perpendicular to it. (ii) $\theta \neq 0$ or π , with $\phi = p\pi/2$ ($p \in \{0, 1, 2, 3\}$). One SNL becomes gapped, while the other remains gapless. (iii) When $\theta \neq 0$ or π , and $\phi \neq p\pi/2$. In these general cases, both SNLs become gapped while two FWPs emerge [illustrated in Fig. 1(d)], positioned at

$$\mathbf{k}_w = \pm \frac{(eA_0) \sin \theta}{\sqrt{2}} (\sin \phi, \cos \phi, 0). \quad (7)$$

The emergence of FWPs reveals that intersected SNLs host fundamentally distinct physical behavior compared to their isolated counterparts.

The FWPs emerging from intersected SNLs exhibit several striking differences compared to those generated in other systems. Specifically, we observe that: (i) A distinctive scaling of Weyl-point separation (d_w). For FWPs originating from a Dirac point, the separation scales as $d_w \propto A_0^2/\omega$ [42]; For a circular nodal ring, d_w is approximately equal to the ring's diameter [illustrated in Fig. 1(b)] and thus independent of A_0 and ω to the leading order [44–46]; In the present case, the

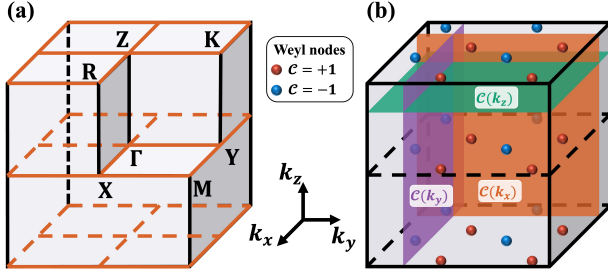


FIG. 2. (a) Red lines mark the locations of the SNLs before driving. (b) Configuration of the emergent FWPs in the driven system, with red and blue dots denoting FWPs of opposite chirality. Note that these FWPs at the top and bottom surfaces belong to the same group due to BZ periodicity. The layer Chern numbers are defined in these gapped planes (color-coded) away from the FWPs.

scaling follows $d_w \propto A_0$, distinguishing it from both Dirac points and nodal rings. (ii) A distinctive dependence of the displacement vector of FWPs on the light's direction. When the light propagates along (ϕ, θ) on the Bloch sphere, the displacement vector aligns with the light direction for the case of Dirac points [42]. For a circular nodal ring, it aligns with $(\phi, \frac{\pi}{2})$, corresponding to the in-plane projection of the light's orientation [44–46], as illustrated in Fig. 1(b). In stark contrast, our analysis [Eq. (7)] reveals that for intersected SNLs, the vector is oriented along $(\frac{\pi}{2} - \phi, \frac{\pi}{2})$, which generally deviates from the light's orientation or its projection, as illustrated in Fig. 1(d).

Linked Fermi arcs.—A defining universal feature of Weyl semimetals is the existence of Fermi arcs in the surface BZ—topological surface states that connect the projections of bulk Weyl points, as required by the bulk-boundary correspondence [40]. Although our continuum Hamiltonian analysis shows that FWPs can emerge from intersected SNLs, determining the connectivity pattern of Fermi arcs and Weyl-point projections requires a lattice-regularized description. We achieve this through the standard lattice regularization substitution $k_i \rightarrow \sin k_i$, which yields the following lattice Hamiltonian:

$$\mathcal{H}(\mathbf{k}) = \sin k_z \sigma_x + \sin k_x \sin k_y \sigma_y. \quad (8)$$

For notational simplicity, we have set the lattice constants to unity. The resulting lattice Hamiltonian supports eight SNLs along high-symmetry lines in the bulk BZ: four in the $k_z = 0$ plane and four in the $k_z = \pi$ plane, as illustrated in Fig. 2(a). Near each of the eight time-reversal invariant momenta where two SNLs intersect, a low-energy expansion yields a continuum Hamiltonian identical in form to Eq. (5), modulo sign differences in the coefficients. This implies that eight pairs of FWPs will emerge under general light irradiation. To verify this prediction, we follow the same analytical procedure and derive the Floquet Hamiltonian, which reads

$$\mathcal{H}_{\text{eff}}(\mathbf{k}) = C \sin k_z \sigma_x + D(\mathbf{k}_s) \cos k_z \sigma_z + F(\mathbf{k}_s) \sigma_y, \quad (9)$$

where $\mathbf{k}_s = (k_x, k_y)$, $C = J_0(\lambda_3 e A_0)$, $F(\mathbf{k}_s) =$

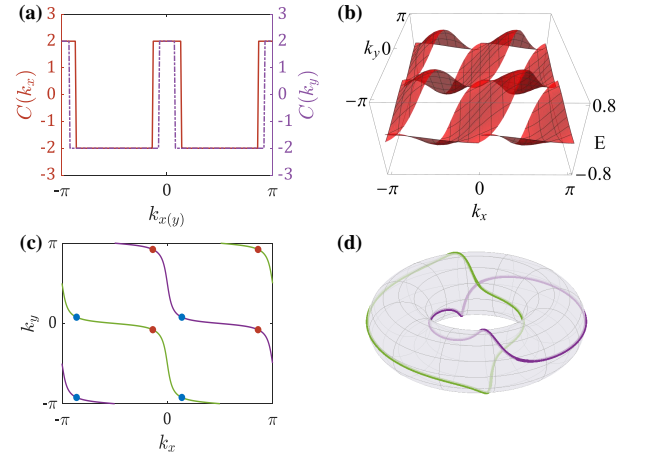


FIG. 3. (a) Momentum-dependence of layer Chern numbers. (b) Surface-state spectrum on the top z -normal surface. (c) Fermi arcs at zero energy (green and purple curves), with red and blue markers indicating Weyl-point projections. (d) Linked topology of Fermi arcs visualized on the surface BZ torus. Parameters are $eA_0 = 0.8$, $\omega = 5$, $\eta = 1$, $\theta = \pi/3$, and $\phi = \pi/3$.

$$-\frac{1}{2} [J_0(\lambda_1 e A_0) \cos k_+ - J_0(\lambda_2 e A_0) \cos k_-], \text{ and}$$

$$D(\mathbf{k}_s) = -2\eta \frac{J_1(\lambda_3 e A_0)}{\omega} [\sin \phi_1 J_1(\lambda_1 e A_0) \sin k_+ - \sin \phi_2 J_1(\lambda_2 e A_0) \sin k_-].$$

Here, we simplify the notation by introducing the following shorthand: $k_{\pm} = k_x \pm k_y$, $\lambda_1 = \sqrt{2 - \sin^2 \theta (\sin 2\phi + 1)}$,

$\lambda_2 = \sqrt{2 + \sin^2 \theta (\sin 2\phi + 1)}$, $\lambda_3 = \sin \theta$, $\sin \phi_1 = (\sin \phi - \cos \phi)/\lambda_1$, $\sin \phi_2 = (\sin \phi + \cos \phi)/\lambda_2$, and $J_n(x)$ denotes Bessel functions of the first kind [derivation details are provided in Sec. I of the Supplemental Material (SM) [75]].

The positions of FWPs are simply determined by the zeros of the coefficients in front of the Pauli matrices. Without loss of generality, we focus on a specific case for a detailed analysis. Specifically, we consider light propagating along the direction $(\theta, \phi) = (\frac{\pi}{3}, \frac{\pi}{3})$. The resulting positions and chiralities of FWPs are illustrated in Fig. 2(b). As expected, we observe four pairs of FWPs in the $k_z = 0$ plane and another four pairs in the $k_z = \pi$ plane. Notably, the distributions of positions and chiralities in the two k_z planes are identical. Consequently, when the bulk Weyl points are projected along the z direction, those with the same topological charge overlap, yielding a net topological charge of $+2$ or -2 per Weyl-point projection. Each Weyl-point projection is thus accompanied by two Fermi arcs, a property we will demonstrate below.

Before identifying the Fermi arcs, we first calculate the momentum-resolved layer Chern number $C(k_i)$ for $i \in \{x, y, z\}$. From the Weyl point distribution in Fig. 2(b), we observe that $C(k_z)$ vanishes identically, whereas $C(k_x)$ and $C(k_y)$ remain nonzero across their respective gapped planes. The explicit momentum dependence of $C(k_x)$ and $C(k_y)$ are plotted in Fig. 3(a). Notably, both $|C(k_x)|$ and $|C(k_y)|$ take

the value 2, signifying that under open boundary conditions along the z direction, two chiral Fermi arcs emerge for any fixed k_x or k_y . Consequently, the Fermi arcs span the entire surface BZ along both k_x and k_y . Intriguingly, $C(k_x)$ and $C(k_y)$ undergo sign reversal across planes containing Weyl points of identical chirality. This behavior demonstrates that the chirality of the Fermi arcs is momentum-dependent, flipping sign at Weyl-point projections—a sharp contrast to 3D Chern insulators [71, 76, 77], where the layer Chern numbers remain constant along a given direction, resulting in a surface-state Fermi loop of fixed chirality. In the present system, we find that a 3D Chern insulator phase can also be realized by further increasing the light amplitude to annihilate all FWPs (see Sec. III of the SM [75]).

The unique momentum dependence of $C(k_x)$ and $C(k_y)$ indicates that the Fermi arcs on the z -normal surfaces will exhibit a linked configuration. To demonstrate this, we need to determine the spectrum of the surface states. This can be done by numerically calculating the energy spectrum for a sample with periodic boundary conditions in the x and y directions and open boundary conditions in the z direction (see Sec. II of the SM [75]). Notably, for the current Hamiltonian, the surface-state spectra can be analytically obtained as the Floquet Hamiltonian in Eq. (9) takes a form similar to the Su-Schrieffer-Heeger model in the z direction [78]. Specially, the surface-state spectra for the top (+) and bottom (−) z -normal surfaces are given by

$$E_{\pm}(\mathbf{k}_s) = \mp \text{sgn}(CD(\mathbf{k}_s))F(\mathbf{k}_s), \quad (10)$$

where the function $\text{sgn}(x)$ equals 1 (−1) for $x > 0$ ($x < 0$). Fig. 3(b) displays the spectrum for the top surface. By tracing the zero-energy contours and Weyl-point projections, we obtain the connectivity of the Fermi arcs, as depicted in Fig. 3(c). Indeed, each Weyl-point projection connects to two Fermi arcs, one from each side. Interestingly these Fermi arcs collectively span the entire surface BZ. When the 2D surface BZ is compactified into a torus by identifying opposite boundaries, the Fermi arcs clearly organize into two mutually linked loops, as illustrated in Fig. 3(d). While Fermi arcs spanning the entire surface BZ have been experimentally observed in chiral topological semimetals [79–82], the linked structure we find here represents a novel feature that has not been previously identified in either static or Floquet Weyl semimetals.

Light-induced anomalous Hall effect.—The emergence of FWPs also leads to the anomalous Hall effect. This light-induced anomalous Hall effect has been experimentally observed in various Dirac semimetals under CPL irradiation, including 2D graphene [83] and 3D $\text{Co}_3\text{Sn}_2\text{S}_2$ [84]. Since the system is driven out of equilibrium, we employ the non-equilibrium Floquet Green’s function method to calculate the Hall current and conductivity [1, 72, 85]. Specially, we consider a system of size $N = N_x N_y N_z$, where N_i denotes the number of lattice sites along the i -th direction. A bias voltage V is applied along the z direction, requiring open boundary conditions in z , while periodic boundary conditions are imposed along the x and y directions for computation simplicity.

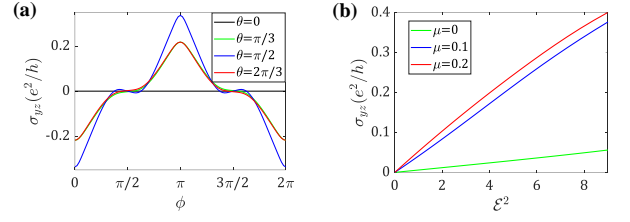


FIG. 4. Zero-temperature Hall conductivity. (a) Hall conductivity σ_{yz} as a function of the light’s propagation direction, calculated for $\mu = 0$ with parameter $eA_0 = 0.8$. (b) σ_{yz} as a function of the light’s intensity, with $\theta = \pi/3$, and $\phi = 5\pi/6$. Common parameters are $\omega = 5$, $\eta = 1$, $V = 0.1$, $\Gamma = 0.2$, and $N_x \times N_y \times N_z = 40 \times 40 \times 10$.

ity. The coupling between the sample and electrodes is set as constant Γ . Here, we focus on the light-induced Hall current along the y direction, as the original static Hamiltonian possesses C_{4z} rotation symmetry. The time-average dc Hall current over one period is given by (with $e = \hbar = 1$)

$$J^y = -\frac{i}{N} \sum_{k_x, k_y} \int_0^\omega \frac{d\varepsilon}{2\pi} \text{Tr}[G_{nm,ij}^<(\varepsilon, \mathbf{k}_s) v_{mn,ji}^y(\mathbf{k}_s)], \quad (11)$$

where $G_{nm,ij}^<$ is the Floquet lesser Green’s function and $v_{mn,ji}^y(\mathbf{k}_s)$ is the Floquet velocity matrix elements (see the End Matter for details). The indices $\{n, m\}$ label the sector in the frequency space, while $\{i, j\}$ label lattice sites along the z direction. Repeated indices are implicitly summed over. Once the current is determined, the Hall conductivity σ_{yz} is calculated as $\sigma_{yz} = J_y/E_z = J_y N_z/V$.

Figure 4(a) shows the evolution of the Hall conductivity σ_{yz} as a function of the light’s propagation direction. Notably, σ_{yz} vanishes identically when $\theta = 0$ (and equivalently for $\theta = \pi$), since CPL perpendicular to SNLs cannot induce FWPs and preserves \mathcal{PT} symmetry in this configuration. Interestingly, σ_{yz} also remains zero at $\phi = \pi/2$ and $\phi = 3\pi/2$, corresponding to light incident along the angular bisector of the perpendicularly crossed SNLs. In these cases, the FWPs are symmetrically distributed, resulting in a complete cancellation of their contributions to the Hall conductivity. These findings demonstrate a strong dependence of σ_{yz} on the light’s orientation. In Fig. 4(b), we further analyze the evolution of σ_{yz} with respect to the light intensity, expressed as \mathcal{E}^2 , where $\mathcal{E} = \omega A_0$ is the electric field amplitude). Within the weak intensity regime, the Hall conductivity exhibits a linear dependence on the light intensity. This linear behavior is universal regardless of the chemical potential μ . However, tuning μ can strongly affects the slope of the linear dependence, as shown in Fig. 4(b).

Discussions and conclusions.—We have demonstrated that CPL can controllably generate FWPs from intersected SNLs. This discovery advances our fundamental understanding of light-driven topological transitions between nodal-line semimetals and Weyl semimetals, while revealing a novel Weyl semimetal phase characterized by linked Fermi arcs. Beyond enabling momentum-dependent chiral transport, these linked Fermi arcs are expected to host exotic transport phe-

nomena under magnetic fields. This arises because the linking structure produces unique Weyl orbitals [86]—the electron’s isoenergy trajectories in a magnetic field—as multiple closed paths become available. Consequently, we anticipate the emergence of exotic signatures in quantum oscillations [87, 88] and 3D quantum Hall effects [89–91] tied to these Weyl orbitals.

Although intersected SNLs can appear in nonmagnetic and magnetic materials, here we highlight the relevance of our theoretical predictions to spin-splitting antiferromagnets—a class of materials exhibiting momentum-dependent spin splitting and symmetry-enforced zero-net magnetization [92–100]. The underlying symmetries responsible for these characteristics naturally stabilize SNLs along high symmetry lines in the BZ [66, 70]. Notably, recent theoretical work has identified several existing compounds—including $\beta\text{-Fe}_2(\text{PO}_4)\text{O}$, $\text{Co}_2(\text{PO}_4)\text{O}$ and LiTi_2O_4 —as altermagnets hosting such intersected SNLs [67]. Based on our study, a light-induced topological transition from SNLs to Weyl points can be probed by TrARPES in these materials. Beyond quantum materials, the predicted Weyl phase characterized by linked Fermi arcs also offers exciting opportunities for investigating unconventional bulk-boundary physics in classical systems [101–106]. The minimal two-band Hamiltonian in Eq. (9) also serves as an ideal model for experimental exploration due to its simplicity, enabling direct implementation in classical systems.

Acknowledgements.—This work is supported by the National Natural Science Foundation of China (Grant No. 12174455), and Guangdong Basic and Applied Basic Research Foundation (Grant No. 2023B1515040023).

* yanzhb5@mail.sysu.edu.cn

- [1] T. Oka and H. Aoki, Photovoltaic Hall effect in graphene, *Phys. Rev. B* **79**, 081406 (2009).
- [2] T. Kitagawa, E. Berg, M. Rudner, and E. Demler, Topological characterization of periodically driven quantum systems, *Phys. Rev. B* **82**, 235114 (2010).
- [3] N. H. Lindner, G. Refael, and V. Galitski, Floquet topological insulator in semiconductor quantum wells, *Nature Physics* **7**, 490 (2011).
- [4] L. Jiang, T. Kitagawa, J. Alicea, A. R. Akhmerov, D. Pekker, G. Refael, J. I. Cirac, E. Demler, M. D. Lukin, and P. Zoller, Majorana Fermions in Equilibrium and in Driven Cold-Atom Quantum Wires, *Phys. Rev. Lett.* **106**, 220402 (2011).
- [5] M. S. Rudner, N. H. Lindner, E. Berg, and M. Levin, Anomalous Edge States and the Bulk-Edge Correspondence for Periodically Driven Two-Dimensional Systems, *Phys. Rev. X* **3**, 031005 (2013).
- [6] A. G. Grushin, A. Gómez-León, and T. Neupert, Floquet Fractional Chern Insulators, *Phys. Rev. Lett.* **112**, 156801 (2014).
- [7] A. C. Potter, T. Morimoto, and A. Vishwanath, Classification of Interacting Topological Floquet Phases in One Dimension, *Phys. Rev. X* **6**, 041001 (2016).
- [8] F. Harper and R. Roy, Floquet Topological Order in Interacting Systems of Bosons and Fermions, *Phys. Rev. Lett.* **118**, 115301 (2017).
- [9] R. Roy and F. Harper, Periodic table for Floquet topological insulators, *Phys. Rev. B* **96**, 155118 (2017).
- [10] S. Yao, Z. Yan, and Z. Wang, Topological invariants of Floquet systems: General formulation, special properties, and Floquet topological defects, *Phys. Rev. B* **96**, 195303 (2017).
- [11] T. Morimoto, H. C. Po, and A. Vishwanath, Floquet topological phases protected by time glide symmetry, *Phys. Rev. B* **95**, 195155 (2017).
- [12] T. Oka and S. Kitamura, Floquet engineering of quantum materials, *Annual Review of Condensed Matter Physics* **10**, 387 (2019).
- [13] M. S. Rudner and N. H. Lindner, Band structure engineering and non-equilibrium dynamics in Floquet topological insulators, *Nature Reviews Physics* **2**, 229 (2020).
- [14] C. Bao, P. Tang, D. Sun, and S. Zhou, Light-induced emergent phenomena in 2D materials and topological materials, *Nature Reviews Physics* **4**, 33 (2022).
- [15] F. Zhan, R. Chen, Z. Ning, D.-S. Ma, Z. Wang, D.-H. Xu, and R. Wang, Perspective: Floquet engineering topological states from effective models towards realistic materials, *Quantum Frontiers* **3**, 21 (2024).
- [16] Y. Wang, H. Steinberg, P. Jarillo-Herrero, and N. Gedik, Observation of Floquet-Bloch states on the surface of a topological insulator, *Science* **342**, 453 (2013).
- [17] S. Zhou, C. Bao, B. Fan, H. Zhou, Q. Gao, H. Zhong, T. Lin, H. Liu, P. Yu, P. Tang, S. Meng, W. Duan, and S. Zhou, Pseudospin-selective Floquet band engineering in black phosphorus, *Nature* **614**, 75 (2023).
- [18] D. Choi, M. Mogi, U. De Giovannini, D. Azoury, B. Lv, Y. Su, H. Hübener, A. Rubio, and N. Gedik, Observation of Floquet-Bloch states in monolayer graphene, *Nature Physics* **10.1038/s41567-025-02888-8** (2025).
- [19] N. Bielinski, R. Chari, J. May-Mann, S. Kim, J. Zwettler, Y. Deng, A. Aishwarya, S. Roychowdhury, C. Shekhar, M. Hashimoto, D. Lu, J. Yan, C. Felser, V. Madhavan, Z.-X. Shen, T. L. Hughes, and F. Mahmood, Floquet-Bloch manipulation of the Dirac gap in a topological antiferromagnet, *Nature Physics* **21**, 458 (2025).
- [20] C.-K. Chiu, J. C. Y. Teo, A. P. Schnyder, and S. Ryu, Classification of topological quantum matter with symmetries, *Rev. Mod. Phys.* **88**, 035005 (2016).
- [21] J. Cayssol, B. Dóra, F. Simon, and R. Moessner, Floquet topological insulators, *physica status solidi (RRL)-Rapid Research Letters* **7**, 101 (2013).
- [22] G. Usaj, P. M. Perez-Piskunow, L. E. F. Foa Torres, and C. A. Balseiro, Irradiated graphene as a tunable Floquet topological insulator, *Phys. Rev. B* **90**, 115423 (2014).
- [23] Z. F. Wang, Z. Liu, J. Yang, and F. Liu, Light-Induced Type-II Band Inversion and Quantum Anomalous Hall State in Monolayer FeSe, *Phys. Rev. Lett.* **120**, 156406 (2018).
- [24] X. Wan, A. M. Turner, A. Vishwanath, and S. Y. Savrasov, Topological semimetal and Fermi-arc surface states in the electronic structure of pyrochlore iridates, *Phys. Rev. B* **83**, 205101 (2011).
- [25] G. Xu, H. Weng, Z. Wang, X. Dai, and Z. Fang, Chern Semimetal and the Quantized Anomalous Hall Effect in HgCr_2Se_4 , *Phys. Rev. Lett.* **107**, 186806 (2011).
- [26] Z. Wang, Y. Sun, X.-Q. Chen, C. Franchini, G. Xu, H. Weng, X. Dai, and Z. Fang, Dirac semimetal and topological phase transitions in $A_3\text{Bi}$ ($A = \text{Na}, \text{K}, \text{Rb}$), *Phys. Rev. B* **85**, 195320 (2012).
- [27] Z. Wang, H. Weng, Q. Wu, X. Dai, and Z. Fang, Three-dimensional Dirac semimetal and quantum transport in Cd_3As_2 , *Phys. Rev. B* **88**, 125427 (2013).

- [28] B. Bradlyn, J. Cano, Z. Wang, M. G. Vergniory, C. Felser, R. J. Cava, and B. A. Bernevig, Beyond Dirac and Weyl fermions: Unconventional quasiparticles in conventional crystals, *Science* **353**, 10.1126/science.aaf5037 (2016).
- [29] A. A. Burkov, M. D. Hook, and L. Balents, Topological nodal semimetals, *Phys. Rev. B* **84**, 235126 (2011).
- [30] C. Fang, Y. Chen, H.-Y. Kee, and L. Fu, Topological nodal line semimetals with and without spin-orbital coupling, *Phys. Rev. B* **92**, 081201 (2015).
- [31] T. Bzdušek, Q. Wu, A. Rüegg, M. Sigrist, and A. A. Soluyanov, Nodal-chain metals, *Nature* **538**, 75 (2016).
- [32] Q. Yan, R. Liu, Z. Yan, B. Liu, H. Chen, Z. Wang, and L. Lu, Experimental discovery of nodal chains, *Nature Physics* **14**, 461 (2018).
- [33] W. Chen, H.-Z. Lu, and J.-M. Hou, Topological semimetals with a double-helix nodal link, *Phys. Rev. B* **96**, 041102 (2017).
- [34] Z. Yan, R. Bi, H. Shen, L. Lu, S.-C. Zhang, and Z. Wang, Nodal-link semimetals, *Phys. Rev. B* **96**, 041103 (2017).
- [35] R. Bi, Z. Yan, L. Lu, and Z. Wang, Nodal-knot semimetals, *Phys. Rev. B* **96**, 201305 (2017).
- [36] M. Ezawa, Topological semimetals carrying arbitrary Hopf numbers: Fermi surface topologies of a Hopf link, Solomon's knot, trefoil knot, and other linked nodal varieties, *Phys. Rev. B* **96**, 041202 (2017).
- [37] P.-Y. Chang and C.-H. Yee, Weyl-link semimetals, *Phys. Rev. B* **96**, 081114 (2017).
- [38] Q.-F. Liang, J. Zhou, R. Yu, Z. Wang, and H. Weng, Node-surface and node-line fermions from nonsymmorphic lattice symmetries, *Phys. Rev. B* **93**, 085427 (2016).
- [39] W. Wu, Y. Liu, S. Li, C. Zhong, Z.-M. Yu, X.-L. Sheng, Y. X. Zhao, and S. A. Yang, Nodal surface semimetals: Theory and material realization, *Phys. Rev. B* **97**, 115125 (2018).
- [40] N. P. Armitage, E. J. Mele, and A. Vishwanath, Weyl and dirac semimetals in three-dimensional solids, *Rev. Mod. Phys.* **90**, 015001 (2018).
- [41] C.-K. Chan, P. A. Lee, K. S. Burch, J. H. Han, and Y. Ran, When Chiral Photons Meet Chiral Fermions: Photoinduced Anomalous Hall Effects in Weyl Semimetals, *Phys. Rev. Lett.* **116**, 026805 (2016).
- [42] H. Hübener, M. A. Sentef, U. De Giovannini, A. F. Kemper, and A. Rubio, Creating stable Floquet-Weyl semimetals by laser-driving of 3D Dirac materials, *Nature Communications* **8**, 13940 (2017).
- [43] L. Bucciattini, S. Roy, S. Kitamura, and T. Oka, Emergent Weyl nodes and Fermi arcs in a Floquet Weyl semimetal, *Phys. Rev. B* **96**, 041126 (2017).
- [44] Z. Yan and Z. Wang, Tunable Weyl Points in Periodically Driven Nodal Line Semimetals, *Phys. Rev. Lett.* **117**, 087402 (2016).
- [45] C.-K. Chan, Y.-T. Oh, J. H. Han, and P. A. Lee, Type-II Weyl cone transitions in driven semimetals, *Phys. Rev. B* **94**, 121106 (2016).
- [46] A. Narayan, Tunable point nodes from line-node semimetals via application of light, *Phys. Rev. B* **94**, 041409 (2016).
- [47] K. Taguchi, D.-H. Xu, A. Yamakage, and K. T. Law, Photo-voltaic anomalous Hall effect in line-node semimetals, *Phys. Rev. B* **94**, 155206 (2016).
- [48] Z. Yan and Z. Wang, Floquet multi-Weyl points in crossing-nodal-line semimetals, *Phys. Rev. B* **96**, 041206 (2017).
- [49] M. Ezawa, Photoinduced topological phase transition from a crossing-line nodal semimetal to a multiple-Weyl semimetal, *Phys. Rev. B* **96**, 041205 (2017).
- [50] R. Chen, B. Zhou, and D.-H. Xu, Floquet Weyl semimetals in light-irradiated type-II and hybrid line-node semimetals, *Phys. Rev. B* **97**, 155152 (2018).
- [51] X.-L. Du, R. Chen, R. Wang, and D.-H. Xu, Weyl nodes with higher-order topology in an optically driven nodal-line semimetal, *Phys. Rev. B* **105**, L081102 (2022).
- [52] P. Liu, C. Cui, L. Li, R. Li, D.-H. Xu, and Z.-M. Yu, Floquet control of topological phases and Hall effects in Z_2 nodal line semimetals, *Phys. Rev. B* **111**, 235105 (2025).
- [53] D. Zhang, H. Wang, J. Ruan, G. Yao, and H. Zhang, Engineering topological phases in the Luttinger semimetal α -Sn, *Phys. Rev. B* **97**, 195139 (2018).
- [54] S. A. A. Ghorashi, P. Hosur, and C.-S. Ting, Irradiated three-dimensional Luttinger semimetal: A factory for engineering Weyl semimetals, *Phys. Rev. B* **97**, 205402 (2018).
- [55] H. Liu, J.-T. Sun, C. Cheng, F. Liu, and S. Meng, Photoinduced Nonequilibrium Topological States in Strained Black Phosphorus, *Phys. Rev. Lett.* **120**, 237403 (2018).
- [56] T. V. Trevisan, P. V. Arribi, O. Heinonen, R.-J. Slager, and P. P. Orth, Bicircular Light Floquet Engineering of Magnetic Symmetry and Topology and Its Application to the Dirac Semimetal Cd_3As_2 , *Phys. Rev. Lett.* **128**, 066602 (2022).
- [57] Z.-M. Wang, R. Wang, J.-H. Sun, T.-Y. Chen, and D.-H. Xu, Floquet Weyl semimetal phases in light-irradiated higher-order topological Dirac semimetals, *Phys. Rev. B* **107**, L121407 (2023).
- [58] M. Yang, H.-B. Ding, M.-X. Deng, and R.-Q. Wang, Multifold Weyl semimetals under irradiation: The particularity of singlet Weyl points, *Phys. Rev. B* **109**, 165126 (2024).
- [59] S. Huang, F. Zhan, X. Ding, D.-H. Xu, D.-S. Ma, and R. Wang, Controllable Weyl nodes and Fermi arcs from Floquet engineering triple fermions, *Phys. Rev. B* **110**, L121118 (2024).
- [60] B. Pandit and S. Kar, Floquet analysis on an irradiated nodal surface semimetal with non-symmorphic symmetry, *Journal of Physics: Condensed Matter* **37**, 075601 (2024).
- [61] Y. Hirai, S. Okumura, N. Yoshikawa, T. Oka, and R. Shimano, Floquet Weyl states at one-photon resonance: An origin of nonperturbative optical responses in three-dimensional materials, *Phys. Rev. Res.* **6**, L012027 (2024).
- [62] S. Li, Z.-M. Yu, Y. Liu, S. Guan, S.-S. Wang, X. Zhang, Y. Yao, and S. A. Yang, Type-II nodal loops: Theory and material realization, *Phys. Rev. B* **96**, 081106 (2017).
- [63] G. Liu, Y. Jin, Z. Chen, and H. Xu, Symmetry-enforced straight nodal-line phonons, *Phys. Rev. B* **104**, 024304 (2021).
- [64] L. Wu, F. Tang, and X. Wan, Symmetry-enforced band nodes in 230 space groups, *Phys. Rev. B* **104**, 045107 (2021).
- [65] D. Wang, B. Yang, R.-Y. Zhang, W.-J. Chen, Z. Q. Zhang, S. Zhang, and C. T. Chan, Straight Photonic Nodal Lines with Quadrupole Berry Curvature Distribution and Superimaging "Fermi Arcs", *Phys. Rev. Lett.* **129**, 043602 (2022).
- [66] R. M. Fernandes, V. S. de Carvalho, T. Birol, and R. G. Pereira, Topological transition from nodal to nodeless zeeman splitting in altermagnets, *Phys. Rev. B* **109**, 024404 (2024).
- [67] T. He, L. Li, C. Cui, R.-W. Zhang, Z.-M. Yu, G. Liu, and X. Zhang, Quasi-One-Dimensional Spin Transport in Altermagnetic Z^3 Nodal Net Metals, *Phys. Rev. Lett.* **133**, 146602 (2024).
- [68] F. Tang and X. Wan, Group-theoretical study of band nodes and the emanating nodal structures in crystalline materials, *Quantum Frontiers* **3**, 14 (2024).
- [69] W. Wang, M. Yang, W. Chen, X. Wan, and F. Tang, Large Berry curvature effects induced by extended nodal structures: Rational design strategy and high-throughput materials predictions, *arXiv e-prints*, arXiv:2506.03871 (2025), arXiv:2506.03871 [cond-mat.mtrl-sci].

- [70] Z.-Y. Zhuang, D. Zhu, Z. Wu, and Z. Yan, Cartesian Nodal Lines and Magnetic Kramers Weyl Nodes in Spin-Split Antiferromagnets, arXiv e-prints, arXiv:2502.13212 (2025), arXiv:2502.13212 [cond-mat.mes-hall].
- [71] G.-G. Liu, Z. Gao, Q. Wang, X. Xi, Y.-H. Hu, M. Wang, C. Liu, X. Lin, L. Deng, S. A. Yang, P. Zhou, Y. Yang, Y. Chong, and B. Zhang, Topological Chern vectors in three-dimensional photonic crystals, *Nature* **609**, 925 (2022).
- [72] T. Kitagawa, T. Oka, A. Brataas, L. Fu, and E. Demler, Transport properties of nonequilibrium systems under the application of light: Photoinduced quantum hall insulators without Landau levels, *Phys. Rev. B* **84**, 235108 (2011).
- [73] N. Goldman and J. Dalibard, Periodically Driven Quantum Systems: Effective Hamiltonians and Engineered Gauge Fields, *Phys. Rev. X* **4**, 031027 (2014).
- [74] H. Nielsen and M. Ninomiya, Absence of neutrinos on a lattice: (i). proof by homotopy theory, *Nuclear Physics B* **185**, 20 (1981).
- [75] This supplemental material contains three sections: (I) Derivation of the Floquet lattice Hamiltonian; (II) Surface states of the Floquet lattice Hamiltonian; (III) Evolution of Floquet Weyl points and Fermi arcs with the increase of light amplitude.
- [76] C. Devescovi, M. García-Díez, I. Robredo, M. Blanco de Paz, J. Lasa-Alonso, B. Bradlyn, J. L. Mañes, M. G. Vergniory, and A. García-Etxarri, Cubic 3D Chern photonic insulators with orientable large Chern vectors, *Nature Communications* **12**, 7330 (2021).
- [77] L. Yang, X. Xi, Y. Meng, Z. Zhu, Y. Wu, J. Chen, M. Cheng, K. Xiang, P. P. Shum, Y. Yang, H. Chen, J. Li, B. Yan, G.-G. Liu, B. Zhang, and Z. Gao, Three-dimensional acoustic Chern insulators with arbitrary Chern vectors, *Phys. Rev. Res.* **7**, 023280 (2025).
- [78] W. P. Su, J. R. Schrieffer, and A. J. Heeger, Solitons in Polyacetylene, *Phys. Rev. Lett.* **42**, 1698 (1979).
- [79] G. Chang, S.-Y. Xu, B. J. Wieder, D. S. Sanchez, S.-M. Huang, I. Belopolski, T.-R. Chang, S. Zhang, A. Bansil, H. Lin, and M. Z. Hasan, Unconventional Chiral Fermions and Large Topological Fermi Arcs in RhSi, *Phys. Rev. Lett.* **119**, 206401 (2017).
- [80] Z. Rao, H. Li, T. Zhang, S. Tian, C. Li, B. Fu, C. Tang, L. Wang, Z. Li, W. Fan, J. Li, Y. Huang, Z. Liu, Y. Long, C. Fang, H. Weng, Y. Shi, H. Lei, Y. Sun, T. Qian, and H. Ding, Observation of unconventional chiral fermions with long Fermi arcs in CoSi, *Nature* **567**, 496 (2019).
- [81] N. B. M. Schröter, D. Pei, M. G. Vergniory, Y. Sun, K. Manna, F. de Juan, J. A. Krieger, V. Süß, M. Schmidt, P. Dudin, B. Bradlyn, T. K. Kim, T. Schmitt, C. Cacho, C. Felser, V. N. Strocov, and Y. Chen, Chiral topological semimetal with multifold band crossings and long Fermi arcs, *Nature Physics* **15**, 759 (2019).
- [82] D. Takane, Z. Wang, S. Souma, K. Nakayama, T. Nakamura, H. Oinuma, Y. Nakata, H. Iwasawa, C. Cacho, T. Kim, K. Horiba, H. Kumigashira, T. Takahashi, Y. Ando, and T. Sato, Observation of Chiral Fermions with a Large Topological Charge and Associated Fermi-Arc Surface States in CoSi, *Phys. Rev. Lett.* **122**, 076402 (2019).
- [83] J. W. McIver, B. Schulte, F.-U. Stein, T. Matsuyama, G. Jotzu, G. Meier, and A. Cavalleri, Light-induced anomalous Hall effect in graphene, *Nature Physics* **16**, 38 (2020).
- [84] N. Yoshikawa, S. Okumura, Y. Hirai, K. Ogawa, K. Fujiwara, J. Ikeda, A. Ozawa, T. Koretsune, R. Arita, A. Mitra, A. Tsukazaki, T. Oka, and R. Shimano, Light-induced anomalous Hall conductivity in the massive three-dimensional Dirac semimetal $\text{Co}_3\text{Sn}_2\text{S}_2$, *Phys. Rev. B* **111**, 245104 (2025).
- [85] V. Mosallanejad, Y. Wang, and W. Dou, Floquet nonequilibrium Green's function and Floquet quantum master equation for electronic transport: The role of electron-electron interactions and spin current with circular light, *The Journal of Chemical Physics* **160**, 164102 (2024).
- [86] C. Zhang, Y. Zhang, H.-Z. Lu, X. C. Xie, and F. Xiu, Cycling Fermi arc electrons with Weyl orbits, *Nature Reviews Physics* **3**, 660 (2021).
- [87] A. C. Potter, I. Kimchi, and A. Vishwanath, Quantum oscillations from surface Fermi arcs in Weyl and Dirac semimetals, *Nature Communications* **5**, 5161 (2014).
- [88] P. J. W. Moll, N. L. Nair, T. Helm, A. C. Potter, I. Kimchi, A. Vishwanath, and J. G. Analytis, Transport evidence for Fermi-arc-mediated chirality transfer in the Dirac semimetal Cd_3As_2 , *Nature* **535**, 266 (2016).
- [89] C. M. Wang, H.-P. Sun, H.-Z. Lu, and X. C. Xie, 3d quantum hall effect of fermi arcs in topological semimetals, *Phys. Rev. Lett.* **119**, 136806 (2017).
- [90] C. Zhang, A. Narayan, S. Lu, J. Zhang, H. Zhang, Z. Ni, X. Yuan, Y. Liu, J.-H. Park, E. Zhang, W. Wang, S. Liu, L. Cheng, L. Pi, Z. Sheng, S. Sanvito, and F. Xiu, Evolution of Weyl orbit and quantum Hall effect in Dirac semimetal Cd_3As_2 , *Nature Communications* **8**, 1272 (2017).
- [91] C. Zhang, Y. Zhang, X. Yuan, S. Lu, J. Zhang, A. Narayan, Y. Liu, H. Zhang, Z. Ni, R. Liu, *et al.*, Quantum Hall effect based on Weyl orbits in Cd_3As_2 , *Nature* **565**, 331 (2019).
- [92] S. Hayami, Y. Yanagi, and H. Kusunose, Momentum-dependent spin splitting by collinear antiferromagnetic ordering, *Journal of the Physical Society of Japan* **88**, 123702 (2019).
- [93] S. Hayami, Y. Yanagi, and H. Kusunose, Bottom-up design of spin-split and reshaped electronic band structures in antiferromagnets without spin-orbit coupling: Procedure on the basis of augmented multipoles, *Phys. Rev. B* **102**, 144441 (2020).
- [94] L.-D. Yuan, Z. Wang, J.-W. Luo, E. I. Rashba, and A. Zunger, Giant momentum-dependent spin splitting in centrosymmetric low-Z antiferromagnets, *Phys. Rev. B* **102**, 014422 (2020).
- [95] L.-D. Yuan, Z. Wang, J.-W. Luo, and A. Zunger, Prediction of low-Z collinear and noncollinear antiferromagnetic compounds having momentum-dependent spin splitting even without spin-orbit coupling, *Phys. Rev. Mater.* **5**, 014409 (2021).
- [96] P. Liu, J. Li, J. Han, X. Wan, and Q. Liu, Spin-group symmetry in magnetic materials with negligible spin-orbit coupling, *Phys. Rev. X* **12**, 021016 (2022).
- [97] H.-Y. Ma, M. Hu, N. Li, J. Liu, W. Yao, J.-F. Jia, and J. Liu, Multifunctional antiferromagnetic materials with giant piezomagnetism and noncollinear spin current, *Nature Communications* **12**, 2846 (2021).
- [98] L. Šmejkal, J. Sinova, and T. Jungwirth, Beyond Conventional Ferromagnetism and Antiferromagnetism: A Phase with Nonrelativistic Spin and Crystal Rotation Symmetry, *Phys. Rev. X* **12**, 031042 (2022).
- [99] L. Šmejkal, J. Sinova, and T. Jungwirth, Emerging Research Landscape of Altermagnetism, *Phys. Rev. X* **12**, 040501 (2022).
- [100] L. Šmejkal, A. B. Hellenes, R. González-Hernández, J. Sinova, and T. Jungwirth, Giant and Tunneling Magnetoresistance in Unconventional Collinear Antiferromagnets with Nonrelativistic Spin-Momentum Coupling, *Phys. Rev. X* **12**, 011028 (2022).
- [101] M. C. Rechtsman, J. M. Zeuner, Y. Plotnik, Y. Lumer, D. Podolsky, F. Dreisow, S. Nolte, M. Segev, and A. Szameit, Photonic floquet topological insulators, *Nature* **496**, 196

- (2013).
- [102] R. Fleury, A. B. Khanikaev, and A. Alù, Floquet topological insulators for sound, *Nature Communications* **7**, 11744 (2016).
- [103] T. Ozawa, H. M. Price, A. Amo, N. Goldman, M. Hafezi, L. Lu, M. C. Rechtsman, D. Schuster, J. Simon, O. Zilberberg, and I. Carusotto, Topological photonics, *Rev. Mod. Phys.* **91**, 015006 (2019).
- [104] G. Ma, M. Xiao, and C. T. Chan, Topological phases in acoustic and mechanical systems, *Nature Reviews Physics* **1**, 281 (2019).
- [105] W. Zhu, W. Deng, Y. Liu, J. Lu, H.-X. Wang, Z.-K. Lin, X. Huang, J.-H. Jiang, and Z. Liu, Topological phononic metamaterials, *Reports on Progress in Physics* **86**, 106501 (2023).
- [106] Z. Wang, X.-T. Zeng, Y. Biao, Z. Yan, and R. Yu, Realization of a Hopf Insulator in Circuit Systems, *Phys. Rev. Lett.* **130**, 057201 (2023).

End Matter

Since the system under investigation is driven by CPL with frequency $\omega = \frac{2\pi}{T}$, we apply the Floquet non-equilibrium Green's function to calculate the Hall current induced by light. We start from the general two-time Green's function $G(t, t')$, and transform it into the following time-energy Green's function through Fourier transformation:

$$G(t, \varepsilon) = \int_{-\infty}^{\infty} dt' G(t, t') e^{i\varepsilon(t-t')}. \quad (12)$$

Subsequently, as t is a periodic variable, we expand $G(t, \varepsilon)$ with the discrete Fourier series [72],

$$G(t, \varepsilon) = \sum_{n=-N}^N G_n(\varepsilon) e^{-in\omega t}. \quad (13)$$

For the convenience of numerical calculation, however, we instead use another equivalent form that has two Floquet indices m and n to denote the Floquet Green's function $G_{nm}(\varepsilon)$ [85]:

$$G(t, t') = \sum_{n,m} \int_0^\omega \frac{d\varepsilon}{2\pi} e^{-i(\varepsilon+n\omega)t} e^{i(\varepsilon+m\omega)t'} G_{nm}(\varepsilon). \quad (14)$$

$G(t, t')$ could represent any Green's function, such as the retarded/advanced Green's function $G^R(t, t')/G^A(t, t')$, and the lesser/greater Green's function $G^<(t, t')/G^>(t, t')$. The Dyson equation for these Floquet Green's functions are given by [1]:

$$\begin{pmatrix} G^R & G^K \\ 0 & G^A \end{pmatrix}_{mn}^{-1} = \begin{pmatrix} (G_{0;nm}^R & 0 \\ 0 & G_{0;nm}^A) \end{pmatrix} + \Sigma_{mn}, \quad (15)$$

where G^K is the Keldysh Green's function, and these Green's functions satisfy $G^< = (G^R + G^K - G^A)/2$. $G_{0;nm}^{R/A} = (\varepsilon + n\omega \pm i\delta)\delta_{mn} - \mathcal{H}_{mn}$. The term δ denotes an infinitesimal positive constant, and the matrix \mathcal{H}_{mn} is given by $\mathcal{H}_{mn} = \frac{1}{T} \int_0^T e^{im\omega t} \mathcal{H}(t) e^{-in\omega t}$. Σ_{mn} stands for the self energy.

To calculate the light-induced current, we implement a two-terminal model with periodic boundary conditions along both x - and y -directions, while attaching source/drain electrodes along the z -axis. All spin indices are suppressed hereafter unless otherwise specified. We set N_x , N_y and N_z sites in the direction x , y and z , respectively. The dc bias applied to the electrodes is V , with $\mu_L = V/2$ and $\mu_R = -V/2$. The coupling between the sample and electrodes is set as constant Γ , which would be a good approximation for wide-band cases. As previously described, CPL is incident in the direction $\mathbf{n} = (\cos\phi \sin\theta, \sin\phi \sin\theta, \cos\theta)$ and the light amplitude is $A_0 = \mathcal{E}/\omega$, where \mathcal{E} is the electric field amplitude of the CPL and ω is the photon frequency.

Before giving the time-averaged current in a period T , we use the thermodynamic average to calculate the instantaneous current $J(t)$ first, which reads

$$\begin{aligned} J^c(t) &= \text{Tr}[\rho(t)v^c(t)] = \text{Tr}[-iG^<(t, t)v^c(t)] \\ &= \sum_{n,m} \int_0^\omega \frac{d\varepsilon}{2\pi} e^{i(m-n)\omega t} \text{Tr}[-iG_{nm}^<(\varepsilon)v^c(t)], \end{aligned} \quad (16)$$

where we have employed Eq. (14) in the second line, and the superscript c labels the current flow direction. Note that the internal indices k_x , k_y and j (labeling the site in the open-boundary z direction) are made implicit for notational simplicity. The lesser Green's function $G_{nm}^<(\varepsilon)$ is given by [85]:

$$G_{nm}^<(\varepsilon) = \sum_{kl} G_{nk}^R(\varepsilon) \Sigma_{kl}^<(\varepsilon) G_{lm}^A(\varepsilon), \quad (17)$$

where $G^R(\varepsilon)$ and $G^A(\varepsilon)$ can be obtained from Eq. (15). We assume that the electrodes only couple with the sample's outermost layers, leading to Σ_{mn} of the form [1]:

$$\begin{aligned} \Sigma_{mn,ij}(\varepsilon, \mathbf{k}_s) &= \begin{pmatrix} \Sigma_{mn,ij}^R & \Sigma_{mn,ij}^K \\ 0 & \Sigma_{mn,ij}^A \end{pmatrix} \\ &= i\Gamma \delta_{nm} \delta_{i=1,j} \begin{pmatrix} \frac{1}{2} & -1 + 2f_L(\varepsilon + m\omega) \\ 0 & -\frac{1}{2} \end{pmatrix} \\ &\quad + i\Gamma \delta_{nm} \delta_{i,j=N_z} \begin{pmatrix} \frac{1}{2} & -1 + 2f_R(\varepsilon + m\omega) \\ 0 & -\frac{1}{2} \end{pmatrix}. \end{aligned} \quad (18)$$

Accordingly, we have $\Sigma_{mn,ij}^<(\varepsilon, \mathbf{k}_s) = (\Sigma_{mn,ij}^R + \Sigma_{mn,ij}^K - \Sigma_{mn,ij}^A)/2 = i\Gamma \delta_{nm} [\delta_{i=1,j} f_L(\varepsilon + m\omega) + \delta_{i,j=N_z} f_R(\varepsilon + m\omega)]$. Here, $f_r(\varepsilon) = 1/[e^{\beta(\varepsilon - \mu_r)} + 1]$ (where $r = L, R$) is the Fermi-Dirac distribution function for the left (L) and right (R) reservoirs. Due to the finite system size along the x and y directions, the momentum components are discretized as: $k_x = \frac{2p\pi}{N_x}$ with $p \in \{0, 1, \dots, N_x - 1\}$ and $k_y = \frac{2q\pi}{N_y}$ with $q \in \{0, 1, \dots, N_y - 1\}$. The operator $v_{ij}^c(\mathbf{k}_s, t)$ represents the velocity matrix elements between sites i, j , which can be obtained by Fourier transforming $v^c(\mathbf{k}, t) = \frac{\partial \mathcal{H}(\mathbf{k}, t)}{\partial \mathbf{k}^c}$ in the direction z . Finally, by averaging over one period, we

obtain the dc current expression:

$$J^c = -\frac{i}{N} \sum_{mn} \sum_{ij} \sum_{k_x, k_y} \int_0^\omega \frac{d\varepsilon}{2\pi} \text{Tr}[G_{nm,ij}^<(\varepsilon, \mathbf{k}_s) v_{mn,ji}^c(\mathbf{k}_s)], \quad (19)$$

where $v_{mn,ji}^c = \frac{1}{T} \int_0^T dt e^{i(m-n)\omega t} v_{ji}^c(t)$, and $N = N_x N_y N_z$. Specially, we focus on J^y , and the corresponding Hall conductivity is given by $\sigma_{yz} = J^y/E_z$, where $E_z = V/N_z$.